Role of grain size and crystallographic texture on tensile behavior induced by sliding mechanism in Ti-6Al-4V alloy

Fatna Benmessaoud, Mohammed Cheikh, Vincent Velay, Vanessa Vidal, Hiroaki Matsumoto

Role of grain size and crystallographic texture on tensile behavior induced by sliding mechanism in Ti-6Al-4V alloy

Fatna Benmessaoud [a], Mohammed Cheikh [b,a,*], Vincent Velay [a], Vanessa Vidal [a], Hiroaki Matsumoto [c]

[a] Université de Toulouse, Mines Albi, ICA (Institut Clément Ader), Campus Jarlard, 81013 Albi cedex 09, France
[b] Université de Toulouse, IUT de Figeac, ICA (Institut Clément Ader), avenue Nayrac F-46100 Figeac, France
[c] Faculty of Engineering and Design Kagawa University, 2217-20, Hayashi-cho, Kagawa 761-0396, Takamatsu, Japan

Keywords:
Ti-6Al-4V
Grain size
Crystallographic texture
Sliding mechanism
Slip traces
Critical resolved shear stress (CRSS)

A B S T R A C T

The aim of this paper is to investigate the coupled effects of grain size and crystallographic texture on the mechanical behavior induced by gliding mechanism in Ti-6Al-4V alloy. Thus, four microstructures of Ti-6Al-4V alloy whose grain size and crystallographic texture are different were examined by tensile tests along the rolling direction at room temperature. In this study, the contribution of gliding on basal $\langle a \rangle$, prismatic $\langle a \rangle$ and pyramidal $\langle c + a \rangle$ plans in the accommodation of plastic strain was estimated by means of a slip trace analysis. The role of the individual grain size and the crystallographic texture was then statistically evaluated. Based on the results of slip trace analysis, numerical optimizations of the Critical Resolved Shear Stress (CRSS) of basal $\langle a \rangle$, prismatic $\langle a \rangle$ and pyramidal $\langle c + a \rangle$ in the four microstructures were then carried out, using transition scale rules and a local behavior model. The results suggest that the mechanical behavior of Ti-6Al-4V is controlled by the activation of slip systems that depend not only on their CRSS but also the initial orientation and size of each individual grain. The low CRSS of prismatic $\langle a \rangle$ slip systems can lead to early activation of these systems in favorably oriented coarse grains. Therefore, a local plastic deformation can be shown. At high levels of loading, increasing the grain size can minimize the crystallographic texture effects by deforming the unfavorably oriented coarse grains. Moreover, based on the results of the numerical optimization, it can be also suggested that the CRSS can decrease with the increase in grain size according to the local Hall–Petch relationship.

1. Introduction

Due to its high specific strength and good fatigue and corrosion resistance, Ti-6Al-4V titanium alloy is very suitable for moderate temperature applications, in particular in the aeronautics and aerospace industries. One of the challenges associated with this material is to improve the prediction of its macroscopic mechanical properties in relation to its microstructural parameters, such as the grain size and the preferred orientation of grains.

The equiaxed Ti-6Al-4V alloy consists of about 90% of α-grains whose crystal lattice is a Hexagonal Closed Packed (HCP) surrounded by about 10% of β-phase that has a Body-Centered Cubic crystal lattice (BCC) [1]. It can thus be assumed that the plastic deformation is mainly accommodated by the α-phase. The presence of aluminum in this alloy limits the role of twinning mechanisms [2,3]. Therefore, plastic strain is dominated by crystallographic sliding, mainly by prismatic and basal slip along the $\langle a \rangle$ direction. Slip on pyramidal planes along the $\langle a \rangle$ direction is significantly harder, and even more difficult on pyramidal planes along the $\langle c + a \rangle$ direction [4–8].

In the equiaxed Ti-6Al-4V alloy, the role of gliding mechanism on the accommodation of the plastic behavior of α-grains can directly depend on two microscopic features:

- The first is the crystallographic texture: a preferred orientation of neighbor grains could generate a localization of plastic deformation by forming zones with soft or hard orientation with respect to the sliding systems [9–12].
- The second is the grain size: the accumulation of mobile dislocations in grain boundaries leads to a stress concentration and therefore to an increase in the yield strength [13–15]. Thus, by decreasing the grain size, the yield strength increases. For most materials, this phenomenon is described by the Hall–Petch relationship [16,17].

* Corresponding author at: Université de Toulouse, IUT de Figeac, ICA (Institut Clément Ader), avenue Nayrac F-46100 Figeac, France.
E-mail address: mcheikh@univ-tlse2.fr (M. Cheikh).

The activation of the slip systems is also conditioned by reaching their Critical Resolved Shear Stress (CRSS). However, in the case of HCP polycrystal materials namely the Ti-6Al-4V alloy, the identification of this parameter remains difficult and only relative values have been estimated in most previous works [4,6,18–20]. Moreover, it is found that the CRSS depends not only on the type of slip system but also on the grain size [21–24]. Inversely to single crystal materials, in the case of polycrystal materials, not only the lattice friction can be considered as a critical parameter to activate the slip systems. The dislocation gliding may encounter other obstacles such as the grain boundaries and the immobile dislocations. For instance, where the grain size is very small, the dislocation gliding is more difficult. In the case of phenomenological modeling, this effect could be quantitatively taken into account through the CRSS using Hall–Petch relationship [25]. Noted that the CRSS may also evolve during loading because of the interaction of dislocations in the primary slip system with the other activated dislocations. This phenomenon could be modeled through isotropic hardening laws [19,23,26–31].

The present investigation aims first to study the coupled effect of grain size and crystallographic texture on the macroscopic behavior of Ti-6Al-4V, then to discuss their role on the activation of sliding systems induced in the α-phase of this alloy. The aim of this work is also to propose a numerical methodology to identify the CRSS of three slip systems: basal $\langle a \rangle$, prismatic $\langle a \rangle$ and pyramidal $\langle c+a \rangle$, in four microstructures whose grain size is different. The effect of the grain size at the local scale can be thus expressed by a phenomenological way. In addition, the local Hall–Petch relationship [16,17] can be optimized. To reach this goal, tensile tests are first performed until fracture and then until 1, 3 and 5% of strain. Slip trace analysis technique are then proposed to identify the contribution of each slip system type in the accommodation of plastic strain. This technique consists in comparing the experimentally observed traces with those potentials determined from the crystallographic orientation of the grains. After that, a statistical methodology developed by Li et al. [18] is adapted to estimate the CRSS ratios between basal $\langle a \rangle$, prismatic $\langle a \rangle$ and pyramidal $\langle c+a \rangle$ slip systems. Finally, a multi-scale numerical optimization, based on the local behavior model of Méric–Cailletaud [32] and the scale transition rule of Berveiller–Zaoui [33] is developed to optimize the absolute CRSS of slip systems types in the four microstructures.

2. Material and methods

2.1. Material

The initial material was received as two bars of an equiaxed Ti-6Al-4V alloy. The first one was provided by the NHK spring company (Japan) as a bar of 12 mm diameter. This microstructure exhibits an Ultra Fine Grain (UFG) morphology with an average grain size of about 0.6 μm and a Strong Texture (ST) with a maximum intensity of 6 times random on the $\{0002\}_\alpha$ pole figure, as shown in (Fig. 1(a)).

The second alloy is a commercial Ti-6Al-4V grade 5 received as a bar of 20 mm diameter. It is characterized by a Fine Grain (FG) morphology ($\approx$ 3 μm) and displays a Weak Texture (WT) characterized by basal planes $\{0002\}_\alpha$ tilted by about $\pm 72°$ from X (RD) towards the Z (ND) direction as shown in Fig. 1(b). The chemical composition of the two microstructures is listed in Table 1. The initial crystallographic textures were determined by Electron Backscatter Diffraction (EBSD). HKL `channel 5` software was used to illustrate the measured crystallographic orientations as pole figures.

2.2. Annealing treatment

To increase the grain size of the two microstructures, the two bars (designated by ST-UFG and WT-FG) were heated from room temperature to 870 °C with aheating speed of 15 °C/min, held at this temperature for different annealing times and cooled down to room temperature in the oven as summarized in Table 2.

Table 1
Chemical composition of the initial microstructures.

Elements (wt%)	Ti	Al	V	C	Fe	H	N	O	Y
ST Microstructure	Base	6.26	4.2	<0.1	0.13	<0.1	0.01	0.14	<0.1
WT Microstructure	Base	5.94	3.95	0.052	0.19	0.0002	0.0075	0.185	0.001

The ST-UFG microstructure underwent two different heat treatments characterized each by a dwelling time of 30 min (HT1) and 16 h (HT2) at 870°. The holding time of the third heat treatment (HT3) applied to the WT-FG microstructure was 10 h. The HT1 and HT2 treatments resulted in two other microstructures with an average α grain size of respectively 3 μm designated by ST-FG (Strong Texture with Fine grains) and 7.5 μm designated by ST-SG (Strong Texture with Standard Grains). A fourth microstructure WT-SG (Weak Texture with Standard Grain) was obtained by applying the HT3 treatment to the WT-FG bar (Fig. 2). The four microstructures ST-UFG , ST-FG, ST-SG and WT-SG are investigated in the next sections.

2.3. Tensile tests

Uniaxial monotonic strain controlled tests were performed using an MTS hydraulic machine with a load capacity of 100 kN. An extensometer with a gauge length of 10 mm is used. A first category of tests were conducted until the failure of specimens with a constant strain rate of 5×10^{-4} s^{-1} , allowing identification of the Ti-6Al-4V monotonic behavior. Each test considered a cylindrical specimen made from one of the four microstructures. In a second category of tensile tests, the specimens with standard microstructures (SG) were examined until a deformation of 1, 3 and 5% for WT-SG and 5% for ST-SG microstructures. In this category of tests, the slip traces were observed and analyzed using EBSD and SEM to enable the study of the evolution of slip activity according to strain levels. To make EBSD measurements and SEM observations possible, the specimens, in this category, were machined in a cylindrical shape with two flat surfaces. It should be noted that these specimens were manually polished and then finished using a liquid composed of 67% of SiC and 33% H_2O_2 for more than one hour.

2.4. Slip trace analysis

The slip trace analysis technique was used to study the activation of the slip systems in the ST-SG and WT-SG microstructures. This technique gives a more accurate prediction of the slip system within each individual grain and therefore explains the impact of the coupled effect of crystallographic texture and grain size on the macroscopic mechanical behavior of Ti-6Al-4V alloy.

Experimental slip traces were observed by SEM after controlled tensile tests and then identified using the orientation data (i.e. Euler angles) provided by EBSD and `ImageJ` software. The identification of the most likely slip systems to be activated was carried out by comparing the results from theoretical slip traces with the experimental ones, as mentioned before. An algorithm was developed to calculate the Schmid factor and slip trace angle of each theoretical slip system according to the loading directions RD. The crystallographic orientation describes the rotation of the principle axes of the crystal e_i^c relative to the principle axes of the specimen e_i^s. Bunge's convention of the three Euler angles (ϕ_1, θ, ϕ_2) was used. It consists of a rotation ϕ_1 about the $e_3^s // Z$ axis followed by a rotation θ around the $e_1^s // X$ axis, then by a third rotation ϕ_2 about the $e_3^s // Z$ axis. ϕ_1 and ϕ_2 vary from 0 to 2π and θ varies from 0 to π. The Schmid factor μ of each potential system s is given by:

$$\mu = (n_s.e_1^s)(d_s.e_1^s) \quad (1)$$

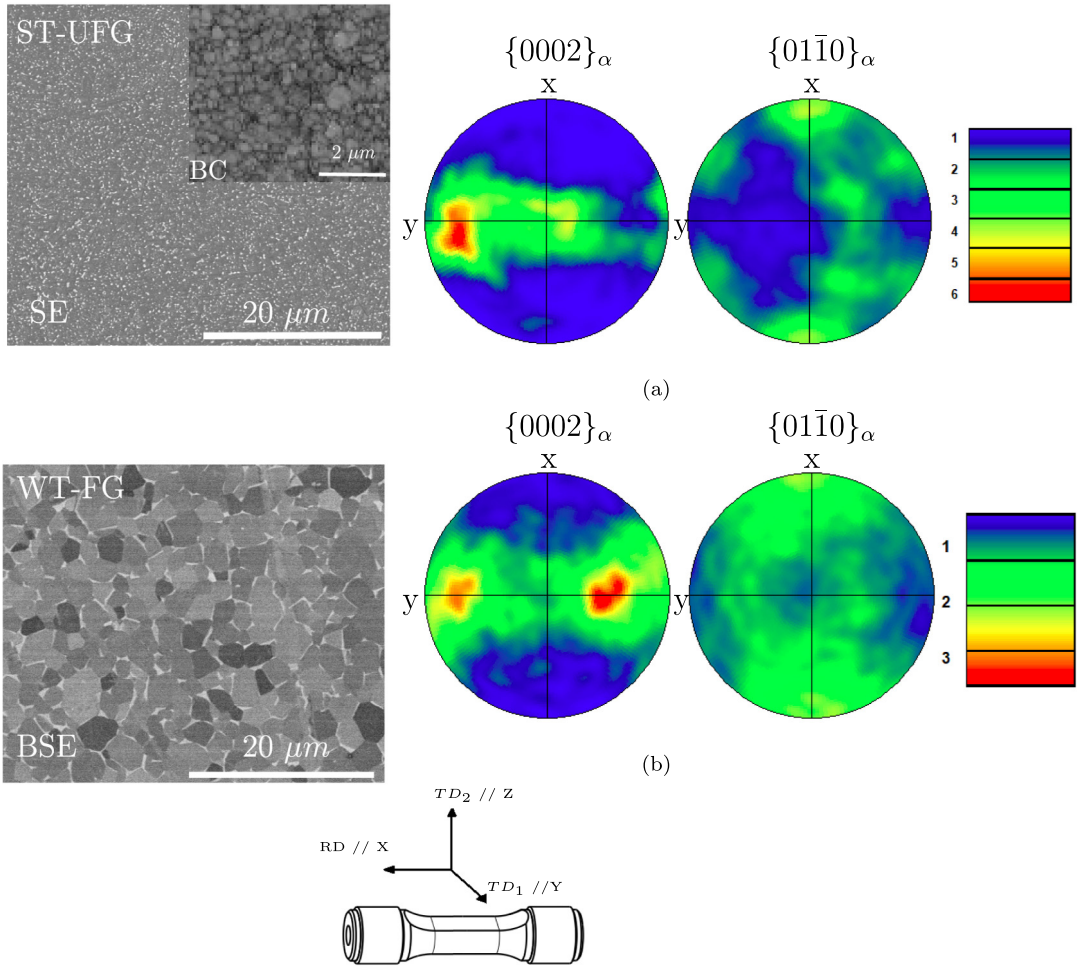

Fig. 1. SEM micrographs of the initial microstructures (left) and their$\{0002\}_\alpha$ and $\{01\bar{1}0\}_\alpha$ pole figures (right): (a) ST-UFG, (b) WT-FG. The enlarged figure defines the UFG grain map of Band Contrast (BC).

Table 2
Designation of the studied microstructures.

Name	Average grain size (μm)	Crystallographic texture	Heat treatment
ST-UFG	0.6 (UFG)	Strongly Textured (ST)	None (As-received)
ST-FG	3 (FG)	Strongly Textured (ST)	HT1: T=870 °C during 30 mn
ST-SG	7.5 (SG)	Strongly Textured (ST)	HT2: T=870 °C during 16 h
WT-FG	2.5 (FG)	Weakly Textured (WT)	None (As-received)
WT-SG	7.5 (SG)	Weakly Textured (WT)	T=870 °C during 10 h

where n_s and d_s are the normal to the slip plane and the slip direction respectively and $e_1^s//X$ is the external load axis. The theoretical angle ψ between the slip trace of slip system s and the tensile axis $e_1^s//X$ is given by:

$$\cos(\psi) = (n_s \wedge e_3^s).e_1^s \tag{2}$$

where $e_3^s//Z$ is the normal to the plane of the specimen. An error of 5° between observed and theoretical traces was accepted. If more than one theoretical slip system lay within ±5° of the experimental slip trace, the slip system exhibiting the highest Schmid factor was selected [5,18,34]. An example of the identification methodology is summarized in Fig. 3.

For the WT-SG microstructure, the slip trace analysis was carried out at strain levels of 1%, 3% and 5%. In this sample the weak texture should give the same opportunity for the activation of several slip systems. Moreover, the slip traces in coarse grains may facilitate the identification of slip traces. For ST-SG, the slip trace analysis was performed only at 5% of strain, to check the effect of crystallographic texture on the slip system activation process.

2.5. Identification of relative and absolute CRSS

2.5.1. Relative CRSS

The activation of a given slip system can be recorded as a function of slip system type (basal $\langle a\rangle$, prismatic $\langle a\rangle$ or pyramidal $\langle c+a\rangle$) and their Schmid factor range. Thus, it was possible to determine the most favorable systems to be activated. In order to eliminate any effect of a preferred orientation of the grain to a slip system type on the determination of the relative values of CRSS, a statistical methodology developed by Li et al. [18] was adapted. For each Schmid factor range j, this method consisted in minimizing the squared difference d between the number of a given slip system type i observed-experimentally O_{ij} and the corresponding expected E_{ij}, giving:

$$d(\tau_1,\tau_2,\tau_3) = \sqrt{\sum_{i=1}^{3}\sum_{j=1}^{m}(\frac{c}{\tau_i}E_{ij} - O_{ij})^2} \tag{3}$$

where $\tau_i (i = 1,2,3)$ are the critical resolved shear stresses of basal (i = 1), prismatic (i = 2) and pyramidal (i = 3) systems respectively. c is an

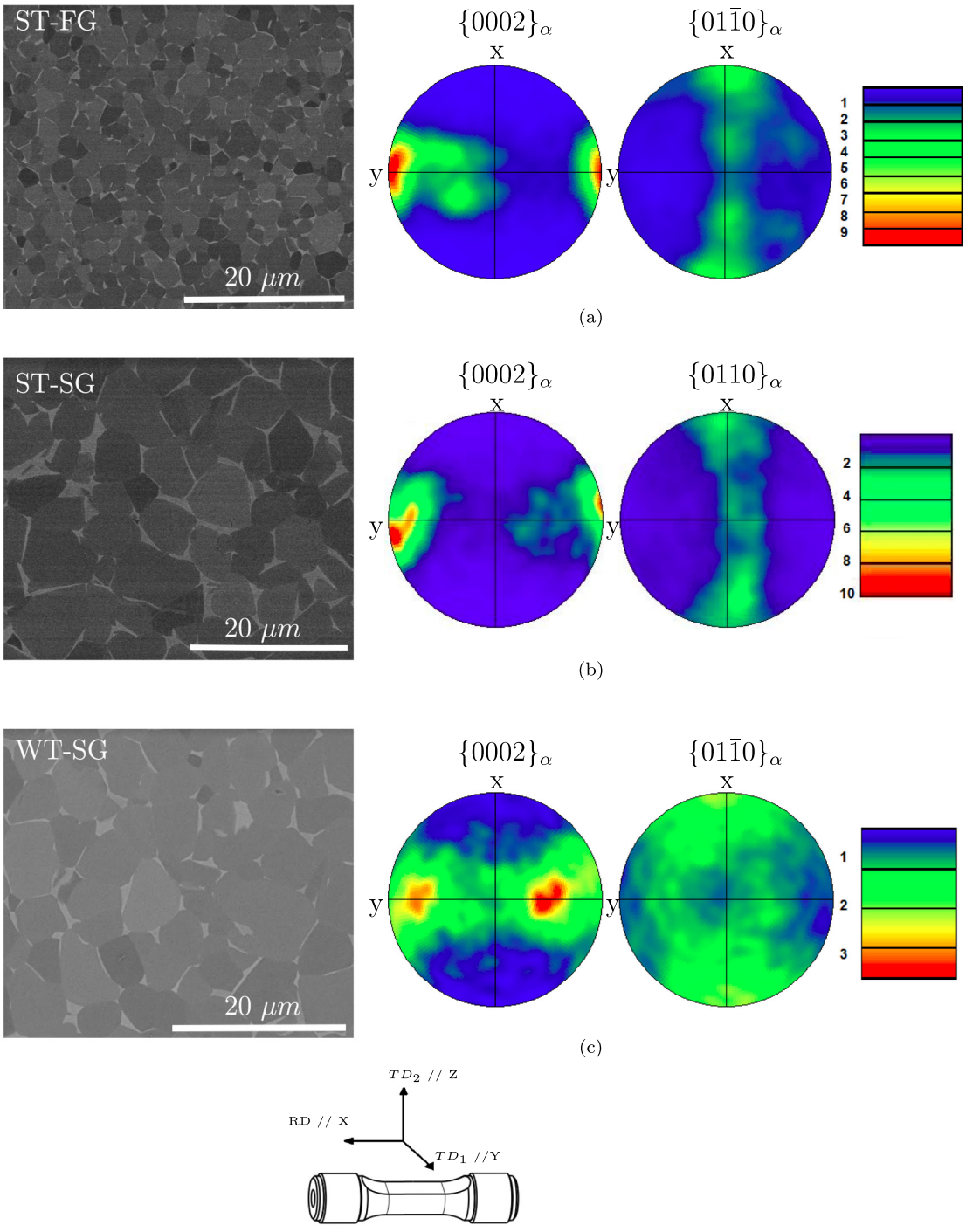

Fig. 2. SEM micrographs of the final microstructures (left) and their $\{0002\}_\alpha$ and $\{01\bar{1}0\}_\alpha$ pole figures (right): (a) ST-UFG, (b) ST-FG, (c) ST-SG, (d) WT-SG.

unknown constant and m is the number of Schmid factor ranges. If all slip systems have the same CRSS, then $\tau_i (i = 1, 2, 3) = c$. The optimal values τ_i^*, which are near a multiplicative constant c for the CRSS values can be computed by solving the first-order derivative conditions for the distance d with respect to τ_1, τ_2 and τ_3 c:

$$\frac{\partial d}{\partial \tau_i} = 0 \longrightarrow \tau_i^* = c \frac{\sum_{j=1}^{m} (E_{ij})^2}{\sum_{j=1}^{m} O_{ij} E_{ij}} \tag{4}$$

Therefore, the relative CRSS ratios to the prismatic value of the prismatic $\langle a \rangle$, basal $\langle a \rangle$ and pyramidal $\langle c + a \rangle$ are given as:

$$\frac{\tau_1^*}{\tau_2^*} : \frac{\tau_2^*}{\tau_2^*} : \frac{\tau_3^*}{\tau_2^*} \tag{5}$$

The advantage of this methodology is that it allows analysis of a large number of grains, making it possible to represent the average behavior by removing the heterogeneity of local stress.

2.5.2. Absolute CRSS

A multi-scale numerical identification of absolute CRSS is proposed in the present section. This optimization uses the obtained relative CRSS, the experimental curves of tensile tests performed until the beginning of plastic behavior, the crystallographic orientations of 500 grains, a local behavior model and the scale transition rule. It consists in finding the coupling values of prismatic, basal and pyramidal CRSS with which the experimental curves of tensile tests can be predicted

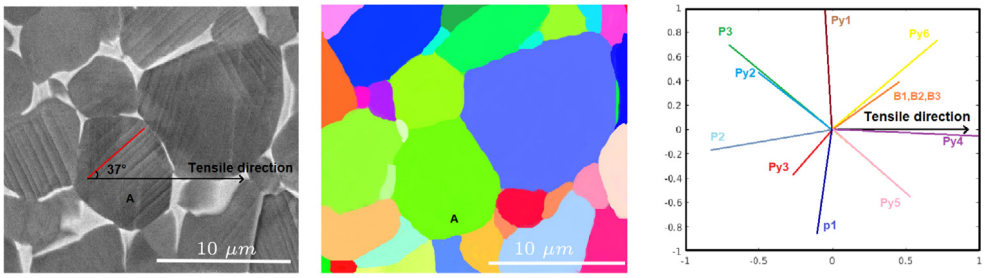

(a) (b) (c)

Type	Slip system number	Slip system	Schmid factor	Trace angle
Basal $\langle a \rangle$	B1	(0001)[-2110]	0.23384	40.74
	B2	(0001)[1-210]	0.3543	40.74
	B3	(0001)[11-20]	0.12055	40.47
Prismatic $\langle a \rangle$	P1	(01-10)[-2110]	0.2695	97.126
	P2	(10-10)[-1-210]	0.1511	168.846
	P3	(-1100)[11-20]	0.41799	135.457
Pyramidal $\langle c+a \rangle$	Py1	(01-11)[-2113]	0.14484	93.065
	Py2	(10-11)[1-213]	0.07716	137.123
	Py3	(-1101)[-1-123]	0.18926	125.446
	Py4	(01-11)[2-1-13]	0.4458	2.978
	Py5	(10-11)[-12-13]	0.025108	45.7356
	Py6	(-1101)[-1-123]	0.009102	43.74

(d)

Fig. 3. An example of slip trace analysis carried out for one grain of WT-SG at 3% of total strain (grain A in this figure): (a) BSE-SEM images, (b) EBSD map orientations, (c) Slip systems traces, (d) Schmid factor values corresponding to the slip systems presented in (c).

correctly and the identified relative CRSS is respected. This procedure is applied to ST-UFG, ST-FG and ST-SG microstructures, with three unknowns CRSS (corresponding to each slip systems type) per optimization. This allows to find for each average grain size (0.6 μm (UFG), 3 μm (FG), 7.5 μm (SG)) the corresponding CRSS of slip systems.

The CRSS are defined through the local model as the unknown parameters of the optimization problem. The transition rule allows the change in scale from the local modeling to macroscopic simulations of the tensile curves. In the optimization procedure, the maximal error that can be accepted between the simulated and the experimental responses is defined. Starting from given initial values of the CRSS of basal $\langle a \rangle$, prismatic $\langle a \rangle$ and pyramidal $\langle c+a \rangle$ systems, the optimizer tries to find optimal values allowing simultaneously to reproduce the experimental curves while respecting the CRSS ratio constraint. By repeating this procedure for each microstructure, the CRSS depending on the grain size can be thus found. The identification procedure is summarized in Fig. 4 and in [35].

Local behavior model. The local behavior model of Méric-Cailletaud [32] is used. It gives a phenomenological description of each slip system behavior. In this model, the slip strain rate $\dot{\gamma}^s$ of system s is given as a form of power function of the resolved shear stress τ^s :

$$\dot{\gamma}^s = \dot{v}^s \text{sign}(\tau^s - \chi^s) \tag{6}$$

with:

$$\dot{v}^s = \left\langle \frac{|\tau^s - \chi^s| - \tau_c^s}{K} \right\rangle^n \tag{7}$$

The $\langle . \rangle$ are Macaulay brackets, defined as: $\langle x \rangle = \begin{cases} 0 & \text{if} \quad 0 \\ x & \text{if} \quad x \geq 0. \end{cases}$ τ_c^s defines the CRSS of the slip system s (s={basal $\langle a \rangle$, prismatic $\langle a \rangle$, pyramidal $\langle c+a \rangle$}). Several CRSS values are considered for each microstructure and introduced in the optimization process. The variables χ^s and r^s are respectively the kinematic and the isotropic hardening variables of slip system s, τ^s is the resolved shear stress of system s, while K and n characterize the material viscosity. Moreover, the nonlinearity of the Ti-6Al-4V hardening can be expressed by the nonlinear kinematic hardening of slip systems according to the Armstrong–Frederick equation: [36]:

$$\chi^s = C\alpha^s \tag{8}$$

with:

$$\dot{\alpha}^s = \dot{\gamma}^s - D\alpha^s \dot{\chi}^s \tag{9}$$

where α^s is a state variable describing the evolution of kinematic hardening in slip system s. C and D are the material parameters. The kinematic hardening and the viscosity parameters determined by Dick et al. [37] are used.

Scale transition rule. Generally, mean field approaches are very relevant in identifying the material parameters at local scale, such as the absolute CRSS. The Berveiller–Zaoui (BZ) model [33] was chosen as a scale transition rule for the identification procedure. For this model, the localization rule of the stress tensor is given by :

$$\sigma = \Sigma + 2G\psi(1-\beta) : (E^p - \varepsilon^p) \tag{10}$$

with:

$$\frac{1}{\psi} = 1 + \frac{3}{2} G \frac{E^p_{\text{eq}}}{\Sigma_{\text{eq}}} \tag{11}$$

and

$$\beta = \frac{2(4-5\nu)}{15(1-\nu)} \tag{12}$$

where σ and Σ are the stresses at the local and the global scales respectively. ε^p and E^p are the local plastic strain and the macroscopic plastic strain. ν is the Poisson ratio, G the shear modulus and ψ stands for a non linear accommodation parameter whose formulation is defined as a function of the Von Mises equivalent inelastic strain E^p_{eq} and stress Σ_{eq} at the macroscopic scale.

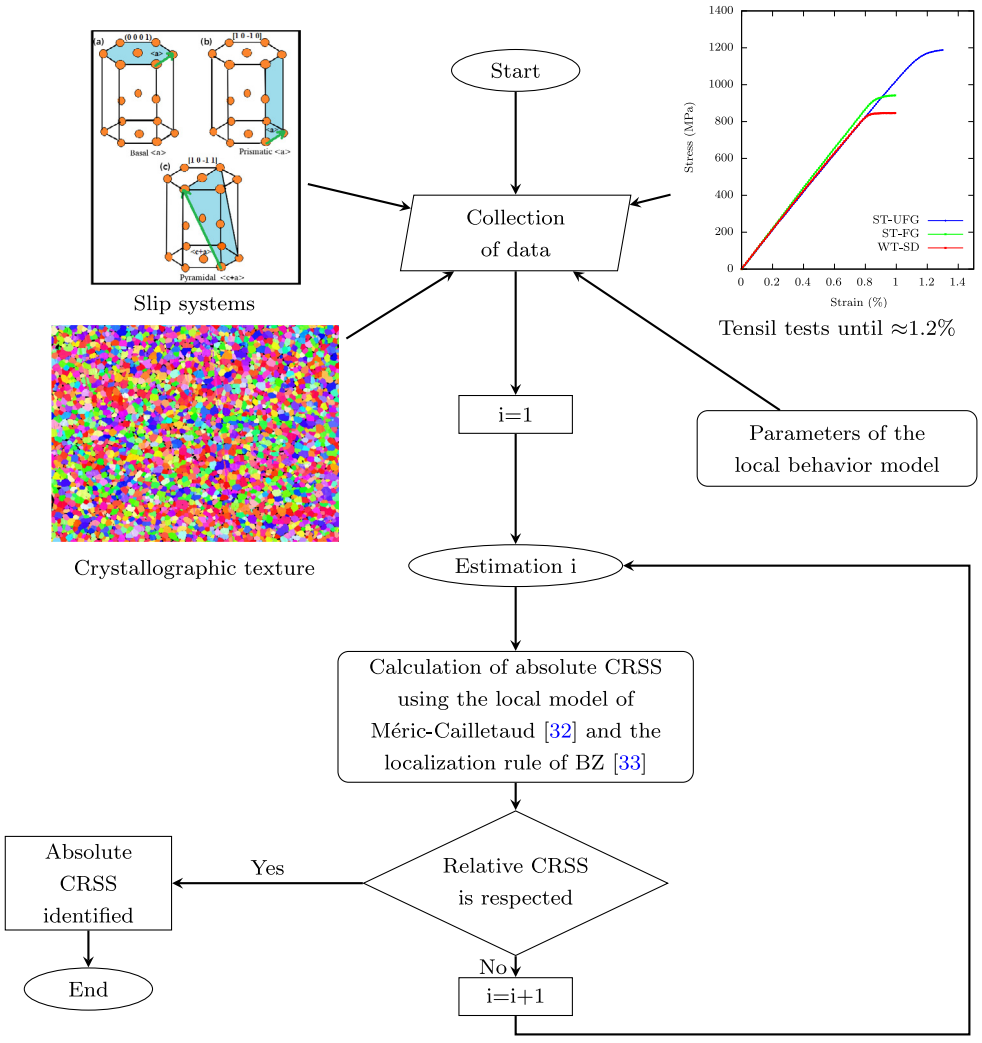

Fig. 4. Optimization procedure of the absolute CRSS.

3. Results

3.1. Tensile behavior

The mechanical behavior of the studied microstructures show an excellent agreement of the elastic responses with a mean Young modulus of 108 GPa. Moreover, ST-SG shows the lowest flow stress, followed by the WT-SG, while ST-UFG presents the highest Yield Strength (YS) and Ultimate Tensile Strength (UTS). WT-SG displays a high ductility with a total Elongation (El) of more than 38% (Table 3). The engineering stress versus engineering strain responses of different ST microstructures are illustrated in Fig. 5(a). The comparison between ST-UFG, ST-FG and ST-SG curves shows a significant influence of α grain size. As expected, yield strength increases and tensile elongation decreases as the average grain size increases from UFG to FG. However, the material keeps the same elongation when grain size increases from FG to SG.

In Fig. 5(b), a comparison between the tensile curves of ST-SG and WT-SG is presented. It can be seen that WT-SG displays the highest ductility and yield strength material. The properties of these two microstructures are reported in Table 3. Moreover, regarding all the curves presented in Fig. 5, it is observed that in ST-UFG microstructure, plasticity occurs without any discontinuous yielding. However, a yield point is shown for ST-FG, ST-SG and WT-SG.

Table 3
Mechanical properties of ST and WT microstructures.

Material	E (GPa)	YS (MPa)	El (%)	UTS (MPa)
ST-UFG	105.982	1190	13	1232
ST-FG	107.142	937	16	995
ST-SG	107.315	843	17	944
WT-SG	113.041	931	≈40	1003

3.2. Activation of slip systems

In ST-SG and WT-SG, more than 200 α-grains were analyzed after strain controlled tensile tests. The slip traces were observed at each strain amplitude as shown in Fig. 6.

After 1% of deformation, about only 5% of grains showed thin slip traces. Evident slip traces appeared after 3% of strain. The resolution of SEM reveals the slip traces only when many dislocations move in the same slip plane. Slip traces in levels less than 1% of strain can be easily observed and defined using SEM-DIC techniques or TEM microscopy (see [38,39]).

The percentage of the yielding grains as well as the activated slip systems after deformation of 1%, 3% and 5% are reported in Table 4. At 3% of deformation, 49% of WT-SG grains present slip traces. This percentage increases to 58% after 5% of total strain. The percentage of

Table 4
Analysis of deformation behavior of tested specimens.

Microstructure	Deformation level (%)	Number of analyzed grains	% of yield grains	% of activated slip systems contribution		
				Basal	Prismatic	Pyramidal
WT-SG	1	138	4.83	39.91	54.31	5.72
	3	205	48.86	35.51	42.06	22.43
	5	230	58.26	34.29	44.02	22.01
ST-SG	5	237	68.68	32.43	37.84	30.27

Table 5
The obtained Hall–Petch parameters in comparison with some literature values.

Material	Grain size range (μm)	k (MPa μm$^{1/2}$)	σ_0 (MPa)	Reference
Ti-6Al-4V	[0.6–7.5]	416	680	Present study
Ti-6Al-4V	[0.8–4]	328	728	[40]
Ti-6Al-4V	[0.6–1.1]	516	440	[41]
Ti-6Al-4V	[0.15–10]	142	942	[42]
CP-Ti[1]	[0.2–10]	269	134	[43]

[1]Commercial pure titanium.

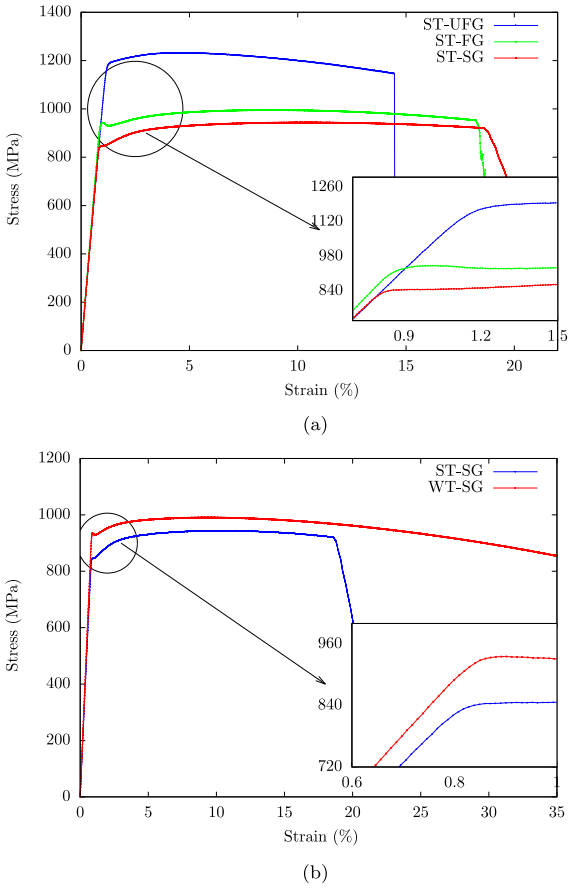

Fig. 5. Stress–Strain curves: (a) Effect of grain size, (b) Effect of crystallographic texture (The legends T1 and T2 correspond to ST and WT respectively in the text).

yielding grains of ST-SG is greater than that of WT-SG, which confirms the macroscopic behavior observed in Fig. 5(b).

Fig. 7 shows the distribution of activated slip systems with respect to their Schmid factor for ST-SG and WT-SG after 5% of deformation. The comparison between slip trace frequency into ST-SG and WT-SG induced by the pyramidal $\langle c+a\rangle$ systems shows that ST-SG was more deformed by this slip system than WT-SG. For both ST-SG and WT-SG, prismatic sliding was detected even when grains were unfavorably oriented (low Schmid factor). About 9% of slip traces refer to prismatic slip with a Schmid factor of less than 0.2, (21% of total prismatic sliding). It should be noted that about 12% of grains present slip traces that do not correspond to the considered slip systems in this study (prismatic $\langle a\rangle$, basal $\langle a\rangle$ and pyramidal $\langle c+a\rangle$). These slip traces may refer to the activation of other sliding systems such as pyramidal $\langle a\rangle$ systems.

4. Discussion

4.1. Macroscopic stress flow dependence on grain size and crystallographic texture

Fig. 8 shows the evolution of the yield strength according to the inverse square root of the average grain size $d^{-1/2}$. The linear Hall–Petch relationship $\sigma_e = kd^{-1/2}+\sigma_0$ can be clearly observed, where k and σ_0 are the Hall Petch slope and the friction lattice stress respectively. The identification of these parameters gives: $k = 416$ MPa μm$^{-1/2}$ and $\sigma_0 = 680$ MPa. In polycrystals, the Hall–Petch relationship claims that dislocations have a slip length limited by the grain boundaries. Therefore, a decrease in the grain size implies an expansion of the grain boundaries area and thus dislocations face more and more obstacles compared with coarse grains. When dislocations pile up at grain boundaries, a large force is required to achieve the plastic flow, which leads to an increase in the yield strength. The obtained values of Hall–Petch parameters in comparison with some values reported in the literature are presented in Table 5. The strong dispersion of these parameters shows that the behavior dependence on grain size can be strongly affected by the producing process, the chemical composition as well as the test conditions.

Due to the strong texture of ST-SG (9 times random in {0002} pole figure), it can be assumed that neighbor α-grains have almost similar orientations. Hence, the dislocations could move more easily through the grains boundaries compared with WT-SG, where dislocations accumulate leading to stress concentrations [44–46]. This can justify the strong yield strength of WT-SG compared with that of ST-SG (Fig. 5(b)). On the other hand, the low ductility of ST-SG may suggest a formation of soft zones surrounded by hard ones. This could induce an increasing of strain mismatches at the grain boundaries between soft and hard oriented grains/zones. Therefore, additional microcracks in these interfaces could be formed [10].

The interpretation of the yield point observed for both ST-FG, ST-SG and WT-SG remains difficult as it requires some nano-scale information from, for example, in-situ-TEM technique that is not the topic of the present investigation. However, it is found from the literature that this phenomenon could be attributed to one of the two following mechanisms [39,47]:

- The first one is related to a limited initial density of mobile dislocations (upper yield point) followed by a rapid multiplication associated to an important dislocations path length. This may lead to a decrease in the stress (lower yield point). Then the material can continue to deform plastically (hardening stage) by the classical mechanisms involving the movement and multiplication of the dislocations as well as their pile-up at the grains boundaries (gradually increase of the yielding grains number).

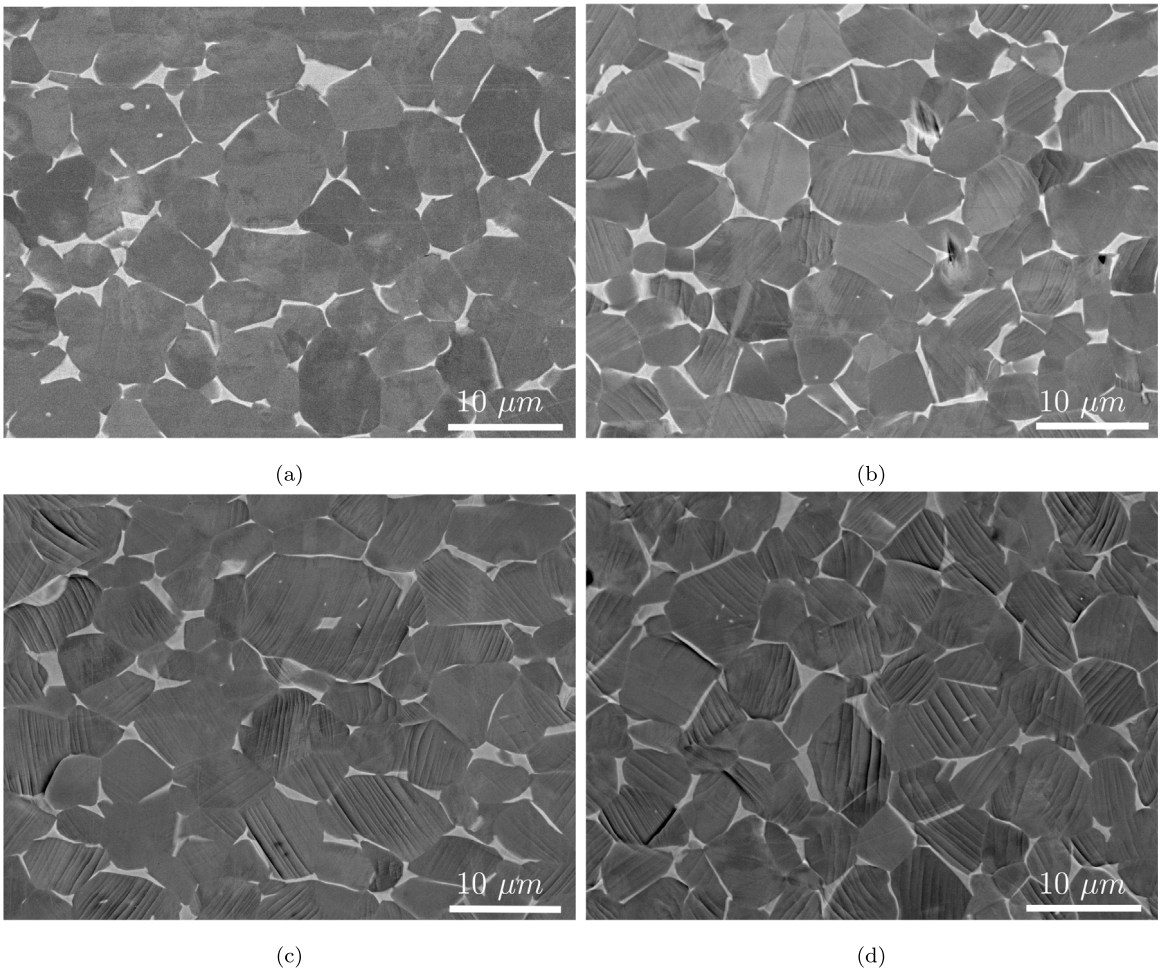

Fig. 6. BSE-SEM micrographs of tensile deformed microstructures: (a) WT-SG at 1%, (b) WT-SG at 3%, (c) WT-SG at 5%, (d) ST-SG at 5%.

- The second mechanism is linked to the insertion of solute elements such as the Oxygen (O) and the Carbon (C). In this case, since these atoms radius are equal or larger than some interstices (octahedral radius interstice in Ti-α), they thus tend to reduce the compression stress which is acting on them by diffusing towards the dislocation sites where there is larger space and form "Cottrel atmosphere". This phenomenon produces strain field at dislocation sites. Some amount of extra stress (upper yield stress) is thus required to tear away the dislocation from this solute rich region. Once they are unpinned, the material comes back to its original position (Lower yield stress) and it requires normal amount of stress to deform.

In Fig. 5, the absence of the yield point in the case of UFG microstructure may be related to the short dislocation path length. In this case, once the dislocations start to move, they could interact the grains boundaries, therefore, the stress decreasing cannot be appear. Noted that the influence of the grain size on the yield point is not well described in the literature.

4.2. Coupled effects of crystallographic texture and grain size on slip activation

Crystallographic slip systems can be activated when their CRSS are exceeded, such that:

$$\tau = \sigma\mu \geq \tau_c \tag{13}$$

where σ is the external stress and μ is the Schmid factor. If all slip systems have the same CRSS, only μ affects their activation. However, for Hexagonal Close Packed materials, the CRSS varies from one slip systems family to another [4,5,20,37,48,49].

The analysis of slip traces suggests that prismatic $\langle a \rangle$ slip is the easiest to be activated, even when its Schmid factor is low (<0.2). It is therefore necessary to understand if only the low CRSS of the prismatic systems are the main cause, as has been reported in the literature [7,8,18,50]. To achieve this, a statistical analysis of the grain size distribution of all deformed grains presenting a prismatic Schmid factor less than 0.2 in WT-SG was performed. Fig. 9(a) shows the distribution of grains presenting the activated Unfavorable Prismatic $\langle a \rangle$ Sliding (UPS) as respect to their size range in WT-SG microstructure. It can be seen that the UPS appears in coarse grains with a size larger than 7.5 μm). For each range of grain size, the ratio between the number of yielding grains (showing UPS) N_y and the total number of grains N_t of this range is defined by $r = N_y/N_t$. This ratio evolution is presented in Fig. 9(b) for each range of grain size. It shows that the ratio for the range between 14 and 16 μm makes the highest contribution in the UPS with about 42%. By decreasing the grain size, the ratio r decreases. This result obtained for prismatic $\langle a \rangle$ systems suggests that the activation of slip systems is associated with local heterogeneous stress concentrations, which depends not only on the CRSS of slip systems and the crystallographic texture but also on the individual grain size. Moreover, several studies have shown that the CRSS itself could be influenced by the grain size. Indeed, increasing of grain size can lead to a decrease in the CRSS [22–25]. It is then necessary to verify this hypothesis in the case of Ti-6Al-4V alloy by identifying the CRSS of different gliding systems for the studied microstructures.

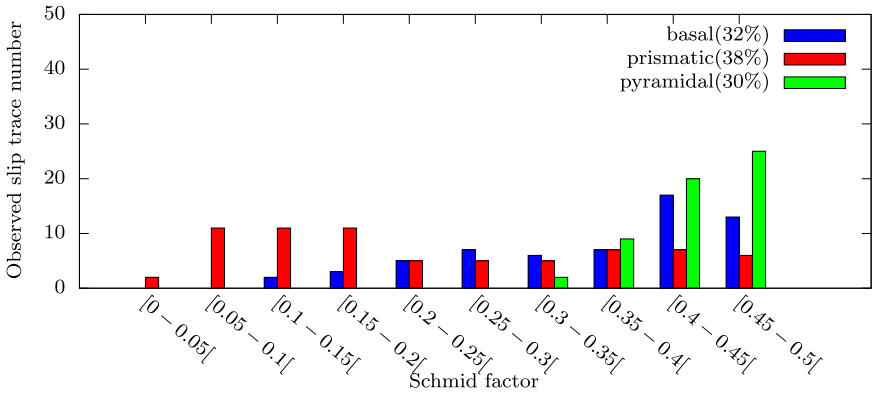

(a)

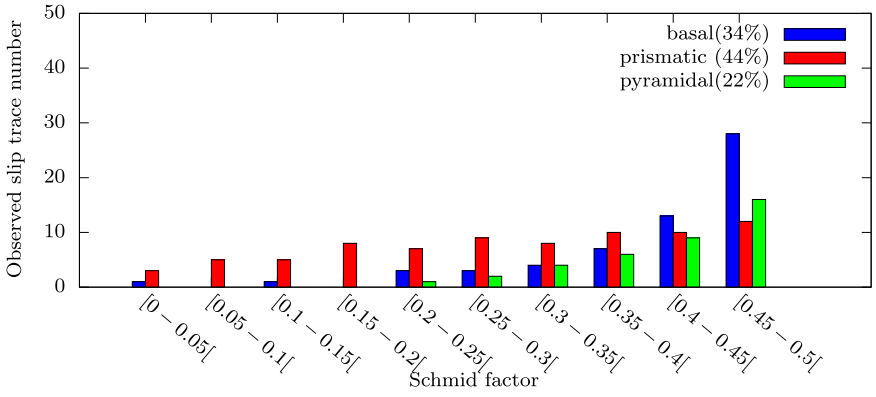

(b)

Fig. 7. Schmid factor distribution of observed slip systems (a) ST-SG at 5%, (b) WT-SG at 5%.

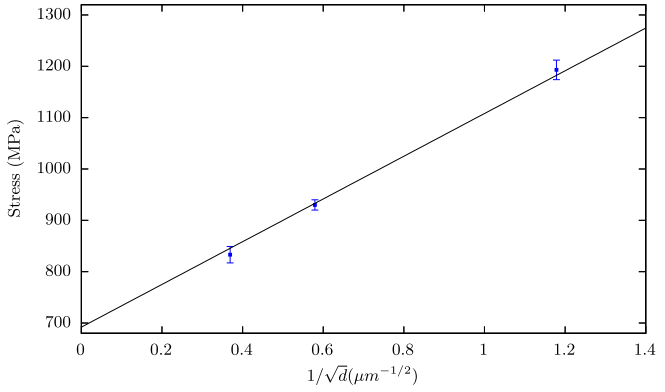

Fig. 8. Hall–Petch relationship between yield strength and inverse square of average grain size.

Table 6
Estimated relative CRSS in comparison with results found in the literature for Ti-6Al-4V.

Basal ⟨a⟩	Prismatic ⟨a⟩	Pyramidal ⟨a⟩	Reference
1.36	1	2.84	Present study
1.05	1	1.68	[37]
1-1.5	1	3–5	[19]
1.43	1	4.23	[20]
0.93–1.3	1	1.1–1.6	[4]

Table 7
Absolute CRSS (in MPa) for basal, prismatic and pyramidal systems.

Material	Basal ⟨a⟩	Prismatic ⟨a⟩	Pyramidal ⟨c + a⟩
ST-UFG	390	290	790
ST-FG	320	240	570
ST-SG	240	170	580
WT-SG	240	170	580

4.3. Identification of relative and absolute CRSS

The relative CRSS was estimated by adapting the methodology developed in [18] as 1.36 : 1 : 2.84 for basal ⟨a⟩, prismatic ⟨a⟩ and pyramidal ⟨c + a⟩ respectively. This result was compared with those found in the literature, as shown in Table 6. It can be observed that the relative CRSS of basal and prismatic slip systems are close in Ti-6Al-4V alloy, in contrast with values for pure titanium [47,51,52]. The addition of aluminum and oxygen elements leads to a reduction in the stacking fault energy on the basal planes, and therefore dislocations are increasingly dissociated and their motion become easier in these planes [8,47].

The identified values of the CRSS are reported in Table 7 and presented then as inverse square root functions of the average grain size (Fig. 10).

The local Hall–Petch slope was found to be 146, 114 and 235 MPa $\mu m^{-1/2}$ for basal, prismatic and pyramidal ⟨c + a⟩ systems respectively. The increase in grain size leads to a decrease in the CRSS, which facilitates the accommodation of plastic strain in coarse grains even when grains are not favorably oriented and confirms the results illustrated in Fig. 9. For the pyramidal ⟨c + a⟩ systems, the high values of CRSS of all Ti-6Al-4V microstructures (Table 7) make the activation of these systems very difficult, even in grains that are favorably

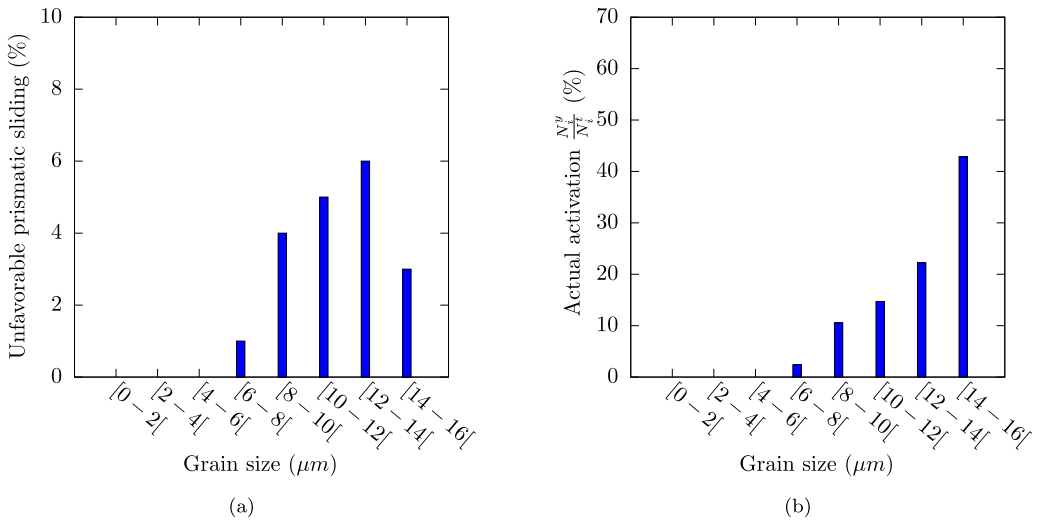

Fig. 9. Distribution of grain size presenting Unfavorable Prismatic Sliding (UPS) with Schmid factor less than 0.2: (a) Observed slip traces, (b) Actual activated systems.

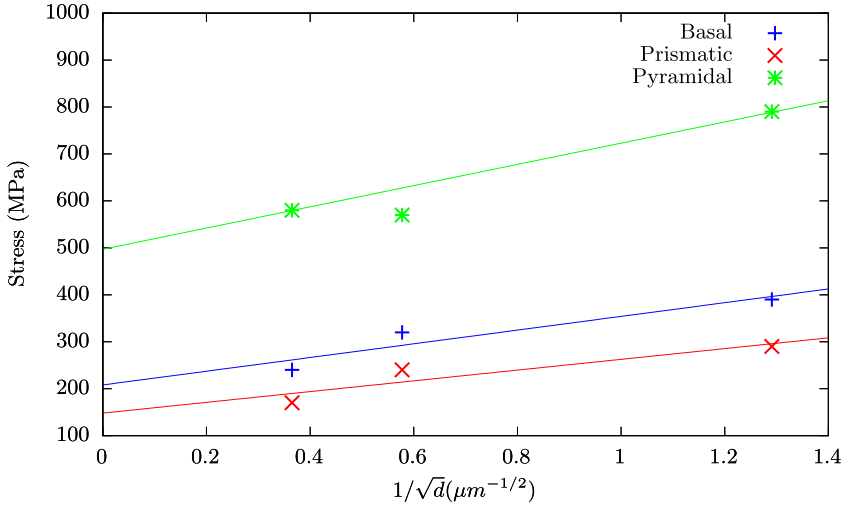

Fig. 10. Evolution of CRSS as function of $1/\sqrt{d}$.

oriented. However, more than 30% of traces in ST-SG and 22% in ST-SG corresponding to these slip systems were observed (Table 4), which may be justified by the existence of grains whose size is much larger than the average grain size (effect of grain size scattering). In addition, the Hall–Petch slope of this sliding type is very high compared with the other systems, which can lead to a significant decrease in pyramidal $\langle c+a \rangle$ CRSS in large grains. In the present study it should also be noted that each grain is considered as an isolated single crystal, thus the effects of interaction between grains, β-phase (10%), dislocations density and the role of grain boundaries as a source of dislocations are not taken into account.

4.4. Estimation of slip system type activation in the four microstructures

To estimate the evolution of the slip system activation in the four microstructures, the Cumulative Distribution Function (CDF) of Schmid factors of more than 2500 grains was determined for each slip system, as shown in Fig. 11. The grains were considered to be favorably oriented for the slip systems when their Schmid factor was higher than 0.4. The similarity of the average Schmid factors of basal $\langle a \rangle$, prismatic $\langle a \rangle$ and pyramidal $\langle c+a \rangle$ systems of WT-SG was observed, which indicates that the same possibilities may be considered to activate these systems. An estimation of the relative amount of activated sliding systems during tensile tests was carried out. This estimation is only based on the Schmid–Boas law Eq. (13) which considers that each grain as an isolated single crystal. The estimated contribution of each slip system type at 5% of deformation is summarized in Table 8. It should be noted that at this amplitude of deformation, the stress is different from one microstructure to another: 1221 MPa for ST-UFG, 976 Mpa for ST-FG, 918 MPa for ST-SG and 982 MPa for WT-SG. By comparing the results of Table 8 with those found experimentally (Table 4), it can be shown that the estimation of the slip system activation in the HCP polycrystal depends not only on the CRSS and the initial crystallographic texture, but also on other parameters such as the interaction between grains and the interaction between slip systems. To take into account all these interactions, it may be necessary to use multi-scale modeling based on local laws and appropriate scale transition methods and introduce the microstructure features as well as the absolute CRSS when estimating the activated slip systems.

5. Summary and conclusions

The influence of the grain size and the crystallographic texture on the mechanical behavior induced by gliding mechanism in Ti-6Al-4V alloy was first investigated at the macroscopic scale. After that, the contribution of basal $\langle a \rangle$, prismatic $\langle a \rangle$ and pyramidal $\langle c+a \rangle$ slip

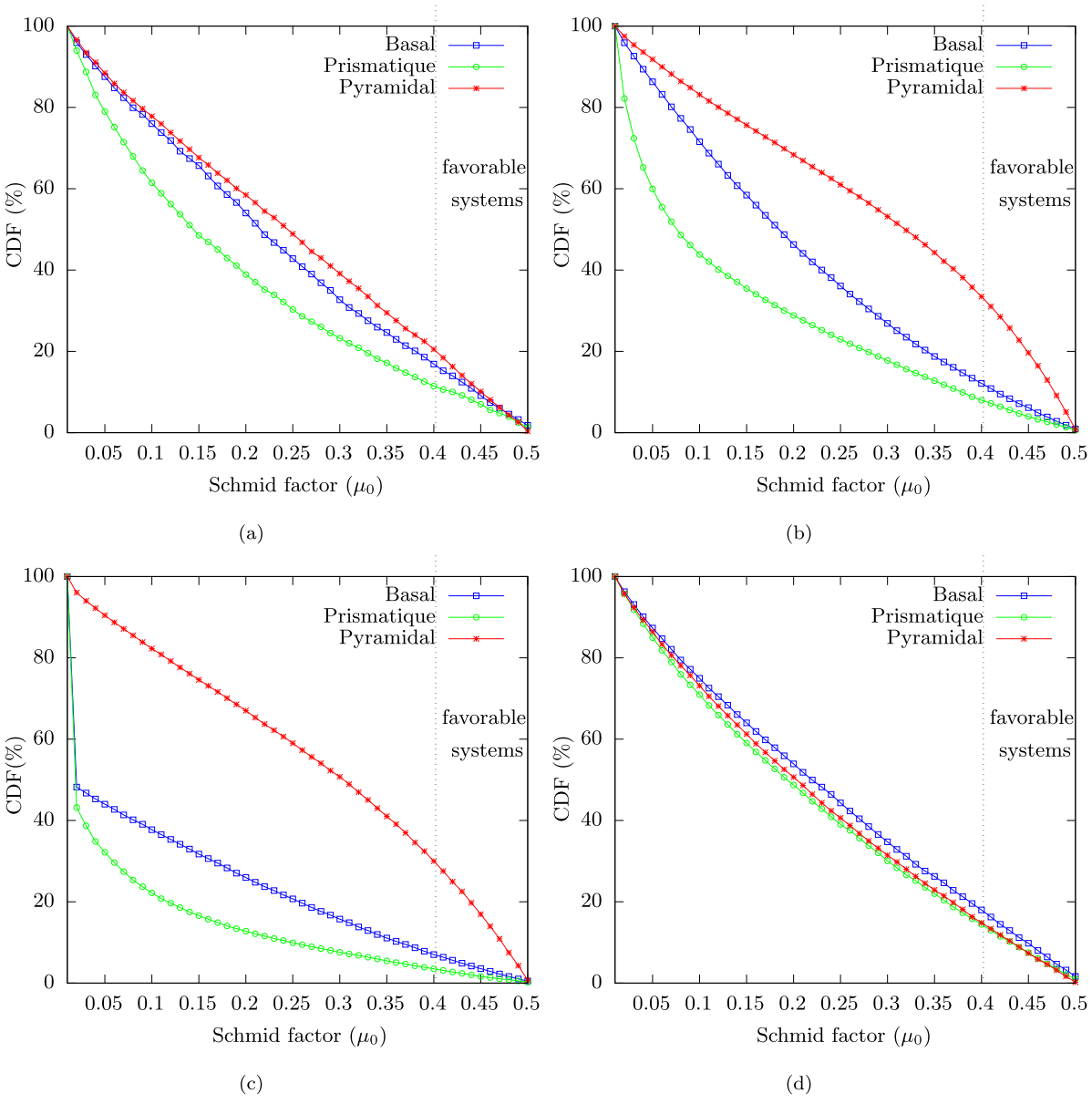

Fig. 11. Cumulative Distribution Function (CDF) of Schmid factor slip systems in: (a) ST-UFG, (b)ST-FG (c) ST-SG, (d) WT-SG.

Table 8
An estimation of activated slip systems number (in %) after 5% of deformation.

Material	Basal $\langle a \rangle$ (%)	Prismatic $\langle a \rangle$ (%)	Pyramidal $\langle c+a \rangle$ (%)
ST-UFG	37	38	0
ST-FG	27	26	0
ST-SG	41	27	6
WT-SG	43	46	4

systems types in relationship with the microstructure features of the material was then evaluated based on slip trace analysis methodology. A statistical methodology followed by numerical optimization were then proposed in order to identify the CRSS of slip systems types in the studied microstructures. Finally, the role of the grain size on the variation of the CRSS of slip systems was discussed. The main conclusions of this research are summarized as follows:

- The significant role of grain size and crystallographic texture on monotonic behavior of Ti-6Al-4V is shown. Increasing the grain size leads to a decrease in the yield strength and an increase in material elongation. A pronounced crystallographic texture leads to a change in the behavior of weakly-textured microstructure according to the loading direction with respect to the c axis of the hexagonal lattice. Strong local anisotropy can therefore appear, which may affect the yield strength and the ductility of the material.
- The contribution of gliding systems on the accommodation of plastic strain shows a dependence on the crystallographic texture. Increasing of Schmid factor for a slip system type facilitates its activation. However, it was observed that prismatic $\langle a \rangle$ and basal $\langle a \rangle$ slip systems are dominant while the pyramidal $\langle c+a \rangle$ slip systems can be activated only with preferred orientation of grains at high level of stress. This result is in agreement with the results found in the literature
- The observation of prismatic $\langle a \rangle$ gliding within coarse grains unfavorably oriented can be related to the low value of prismatic CRSS, especially in coarse grains. Moreover, the numerical optimization of the CRSS of slip systems in the microstructures with Ultra Fine Grains (UFG), Fine Grains (FG) and standard grains

(SG) shows a dependence of the CRSS on grain size that can be expressed by the local Hall–Petch relationship.
- Due to the variety of slip systems in Ti-6Al-4V alloy, their different CRSS and their strong dependence on both the grain size and the initial crystallographic texture, Ti-6Al-4V can present strong plastic heterogeneity at a local scale.

Declaration of competing interest

The authors declare that they have no known competing financial interests or personal relationships that could have appeared to influence the work reported in this paper.

CRediT authorship contribution statement

Fatna Benmessaoud: Writing - review & editing. **Mohammed Cheikh:** Writing - review & editing. **Vincent Velay:** Writing - review & editing. **Vanessa Vidal:** Writing - review & editing. **Hiroaki Matsumoto:** Writing - review & editing.

Acknowledgments

The authors wish to thank the French Occitanie Region for the growth of research activities at the IMT-Mines Albi and Figeac IUT. The authors would also like to gratefully acknowledge the NHK spring company-Japan (https://www.nhkspg.co.jp/eng/) for its support by providing the material used in the study.

References

[1] M.J. Philippe, E. Bouzy, J.J. Fundenberger, Textures and anisotropy of titanium alloys, Mater. Sci. Forum 273–275 (1998) 511–522.
[2] G. Gilles, W. Hammami, V. Libertiaux, O. Cazacu, J.H Yoon, T Kuwabara, A.M Habraken, L Duchêne, Experimental characterization and elasto-plastic modeling of the quasi-static mechanical response of TA6V at room temperature, Solids Struct. 48 (2011) 1277–1289.
[3] W. Tirry, F. Coghe, S. Bouvier, M. Gasperini, L. Rabet, D. Schryvers, A multiscale characterization of deformation twins in Ti-6Al-4V sheet material deformed by simple shear, Mater. Sci. Eng. A 527 (2010) 4136–4145.
[4] J.A. Medina Perilla, J.G. Sevillano, Two-dimensional sections of the yield locus of a Ti-6Al-4V alloy with a strong transverse_type crystallographic a-texture, Mater. Sci. Eng. A 201 (1995) 103–110.
[5] F. Bridier, P. Villechaise, J. Mendez, Analysis of the different slip systems activated by tension in a α/β titanium alloy in relation with local crystallographic orientation, Acta Mater. 53 (2005) 555–567.
[6] D. Dunst, H. Mecking, Analysis of experimental and theoretical rolling textures of two-phase titanium alloys, Z. Met.kd. 87 (1996) 498–507.
[7] A.A Salem, S.R Kalidindi, R.D. Doherty, Strain hardening of titanium: Role of deformation twinning, Acta Mater. 51 (2003) 4225–4237.
[8] S. Zaefferer, A study of active deformation systems in titanium alloys: Dependence on alloy composition and correlation with deformation texture, Mater. Sci. Eng. A 344 (2003) 20–30.
[9] M.E Nixon, O. Cazacu, R.A Lebensohn, Anisotropic response of high-purity α-titanium: Experimental characterization and constitutive modeling, Int. J. Plast. 26 (2010) 516–532.
[10] D. Lunt, Q.D. Fonseca, D. Rugg, M. Preuss, Microscopic strain localisation in Ti-6Al-4V during uniaxial tensile loading, Mater. Sci. Eng. A 680 (2017) 444–453.
[11] H. Fan, S. Aubry, A. Arsenlis, J.A. EL-Awady, Orientation influence on grain size effects in ultrafine-grained magnesium, Scr. Mater. 97 (2015) 25–28.
[12] W.L. Wang, X.L. Wang, W. Mei, J. Sun, Role of grain size in tensile behavior in twinning-induced β Ti-20V-2Nb-2Zr alloy, Mater. Charact. 120 (2016) 263–267.
[13] E. Arzt, Size effects in materials due to microstructural and dimensional constraints: A comparative review, Acta Mater. 46 (1998) 5611–5984.
[14] I.J. Beyerlein, L. Capolungo, P.E. Marshall, R.J. McCabe, C.N. Tome, Statistical analyses of deformation twinning in magnesium, Phil. Mag. 90 (2010) 2161–2190.
[15] A. Fernández, A. Jérusalem, I. Gutiérrez-Urrutia, M.T. Pérez-Prado, Three-dimensional investigation of grain boundary–twin interactions in a Mg AZ31 alloy by electron backscatter diffraction and continuum modeling, Acta Mater. 61 (2013) 7679–7692.
[16] E.O. Hall, The deformation and ageing of mild steel: III discussion of results, Proc. Phys. Soc. B 64 (1951) 747–753.
[17] N.J. Petch, The cleavage strength of polycrystals, J. Iron Steel Inst. 174 (1953) 25–28.
[18] H. Li, D.E. Mason, T.R. Bieler, C.J. Boelert, M.A. Crimp, Methodology for estimating the critical resolved shear stress ratios of α-phase Ti using EBSD-based trace analysis, Acta Mater. 61 (2013) 7555–7567.
[19] J.R. Mayeur, D.L. McDowell, A three-dimensional crystal model for duplex Ti–6Al–4V, Int. J. Plast. 23 (2007) 1457–1485.
[20] S.L. Semiatin, T.R. Bieler, The effect of alpha platelet thickness on plastic flow during hot working of Ti–6Al–4V with a transformed microstructure, Acta Mater. 49 (2001) 3565–3573.
[21] R. Armstrong, I. Codd, R.M. Douthwaite, N.J. Petch, The plastic deformation of polycrystalline aggregates, Phil. Mag. A, J. Theor. Exp. Appl. Phys. (1962) 45–58.
[22] L. Wang, Z. Zheng, H. Phukan, P. Kenesei, J.-S. Park, J. Lind, R.M. Suter, T.R. Bieler, Direct measurement of critical resolved shear stress of prismatic and basal slip in polycrystalline Ti using high energy X-ray diffraction microscopy, Acta Mater. 132 (2017) 598–610.
[23] B. Raeisinia, S.R. Agnew, Using polycrystal plasticity modeling to determine the effects of grain size and solid solution additions on individual deformation mechanisms in cast Mg alloys, Scr. Mater. 63 (2010) 731–736.
[24] C.M. Cepeda-Jiménez, J.M. Molina-Aldareguia, M.T. Pérez-Prado, Effect of grain size on slip activity in pure magnesium polycrystals, Acta Mater. 84 (2015) 443–456.
[25] G.J. Weng, Microstructural theory of grain size dependance in metal plasticity, Int. J. Mech. Phys. Solids 31 (1983) 193–203.
[26] S. Berbenni, V. Favier, M. Berveiller, Impact of the grain size distribution on the behaviour of heterogeneous materials, Int. J. Plast. 23 (2007) 114–142.
[27] N. Nicaise, S. Berbenni, F. Wagner, M. Berveiller, X. Lemoine, Coupled effects of grain size distributions and crystallographic textures on the plastic behaviour of IF steels, Int. J. Plast. 27 (2011) 232–249.
[28] A. Jain, O. Duygulu, D.W. Brown, C.N. Tomé, S.R. Agnew, Grain size effects on the tensile properties and deformation mechanisms of a magnesium alloy, AZ31B, sheet, Mater. Sci. Eng. A 486 (2008) 545–555.
[29] B.S. Fromm, B.L. Adams, S. Ahmadi, M. Knezevic, Grain size and orientation distributions: Application to yielding of α-titanium, Acta Mater. 57 (2009) 2339–2348.
[30] B. Raeisinia, C.W. Sinclair, W.J. Poole, C.N. Tome, On the impact of grain size distribution on the plastic behaviour of polycrystalline metals., Model. Simul. Sci. Eng. 16 (2008) 025001.
[31] B.D. Smith, D. Shih, D.L. McDowell, Cyclic plasticity experiments and polycrystal plasticity modeling of three distinct Ti alloy microstructures, Int. J. Plast. 13 (2018) 1–23.
[32] L. Méric, P. Poubanne, G. Cailletaud, Single crystal modeling for structural calculations: Part 1—Model presentation, Eng. Mater. Technol. 113 (1991) 162–170.
[33] M. Berveiller, A. Zaoui, An extension of the self-consistent scheme to plastically-flowing polycrystals, Mech. Phisycs Solids 26 (1978) 325–344.
[34] S. Hémery, P. Nizou, P. Villechaise, In situ SEM investigation of slip transfer in Ti-6Al-4V: Effect of applied stress, Mater. Sci. Eng. A 709 (2018) 277–284.
[35] A. Nafi, M. Cheikh, O. Mercier, Identification of mechanical properties of CuSil-steel brazed structures joints: A numerical approach, J. Adhes. Sci. Technol. 27 (24) (2013) 2705–2713.
[36] C. Frederick, P. Armstrong, A mathematical representation of the multiaxial bauschinger effect, Mater. High Temp. 24 (2007) 1–26.
[37] T. Dick, G. Cailletaud, Fretting modelling with a crystal model of Ti6Al4V, Comput. Mater. Sci. 38 (2006) 113–125.
[38] M. Kasemer, M.L.P. Echlin, J.C. Stinville, T.M. Pollock, P. Dawsona, On slip initiation in equiaxed α/β Ti-6Al-4V, Acta Mater. 136 (2017) 288–302.
[39] B. Barkia, V. Doquet, J.P. Couzinié, I. Guillot, E. Héripré, In situ monitoring of the deformation mechanisms in titanium with different oxygen contents, Mater. Sci. Eng. A 636 (2015) 91–102.
[40] D.H. Kohn, P. Ducheyne, Tensile and fatigue strength of hydrogen-treated Ti-6Al-4V alloy, Mater. Sci. 26 (1991) 328–334.
[41] Z.X. Zhang, S.J. Qu, A.H. Feng, J. Shen, Achieving grain refinement and enhanced mechanical properties in Ti–6Al–4V alloy produced by multidirectional isothermal forging, Mater. Sci. Eng. A 692 (2017) 127–138.
[42] S. Zherebtsov, E. Kudryavtsev, S. Kostjuchenko, S. Malysheva, G. Salishcheva, Strength and ductility-related properties of ultrafine grained two-phase titanium alloy produced by warm multiaxial forging, Mater. Sci. Eng. A 536 (2012) 190–196.
[43] H.S. Kim, S.J. Yoo, J.W. Ahn, D.H. Kim, W.J. Kim, Ultrafine grained titanium sheets with high strength and high corrosion resistance, Mater. Sci. Eng. A 528 (2011) 8479–8485.
[44] D. Rugg, M. Dixon, F.P.E. Dunne, Effective structural unit size in titanium alloys, Strain Anal. Eng. Design 42 (2007) 269–279.
[45] M.G. Glavicic, B.B. Bartha, S.K. Jha, C.J. Szczepanski, The origins of microtexture in duplex Ti alloys, Mater. Sci. Eng. A 513–514 (2009) 325–328.
[46] L. Germain, N. Gey, M. Humbert, P. Bocher, M. Jahazi, Analysis of sharp microtexture heterogeneities in a bimodal IMI 834 billet, Acta Mater. 53 (2005) 3535–3543.

[47] H. Conrad, Effect of interstitial solutes on the strength and ductility of titanium, Prog. Mater. Sci. 26 (1981) 123–403.
[48] R.A Lebensohn, G.R Canova, A self-consistent approach for modelling texture development of two-phase polycrystals: Application to titanium alloys, Acta Mater. 45 (1997) 3687–3694.
[49] N.E. Paton, J.C. Williams, G.P. Rauscher, The deformation of α-phase titanium, Titan. Sci. Technol. 1 (1973) 1049–1069.
[50] M.J. Philippe, C. Esling, B. Hochheid, Role of twinning in texture development and in plastic deformation of hexagonal materials, Textures Microstruct. 7 (1988) 265–301.
[51] A.T. Churchman, The slip modes of titanium and the effect of purity on their occurrence during tensile deformation of single crystals, Math. Phys. Eng. Sci. 226 (1954) 216–224.
[52] T. Sakai, M. EFine, Plastic deformation of Ti-Al single crystals in prismatic slip, Acta Metall. 22 (1974) 1359–1372.